nature communications

Article

https://doi.org/10.1038/s41467-025-66464-7

Nonvolatile electrical switching of nonreciprocal transport in ferroelectric polar metal WTe_2

Received: 30 September 2025

Accepted: 7 November 2025

Published online: 21 November 2025

Check for updates

Ruihan Wang[1,2,9], Haoyun Chen[1,9], Hui Wang[3,9], Bingyan Liu[1], Xin Chen[1], Jin Cao[4], Ziyi Han[5], Zherui Yang[6], X. Renshaw Wang[1,6], Xiaoxu Zhao[5], Cong Xiao[7], Shengyuan A. Yang[4] ✉ & Peng Song[1,2,8] ✉

Nonreciprocal charge transport in junction-free devices has gained strong research interest recently, due to its capabilities to reveal new quantum physics and potential in outperforming traditional junction-based nonreciprocal devices. While nonreciprocal transport has been reported in a wide range of materials due to various exotic physics, the direction of nonreciprocity is mostly fixed. A key capability that has not been established is the active control of the direction of nonreciprocity. Here by taking advantage of the unique and intrinsic coexistence of switchable ferroelectricity and magnetochiral anisotropy in few-layer polar metal WTe_2, we demonstrate nonvolatile electrical switching of nonreciprocal transport. The direction of nonreciprocal transport is reversed upon electrical switching of the ferroelectric polarization, and the switching is nonvolatile, *i.e.*, it can be maintained even without external voltages. The nonreciprocal transport in few-layer WTe_2 is also highly tunable with electrostatic doping. Theoretical calculations reveal a nontrivial Drude-like mechanism for the reciprocity, with significant band geometrical contribution due to interband coherence. The demonstration of nonvolatile electrically switchable nonreciprocal transport provides a novel route to switch topological quantum physics and paves the way to programmable junction-free diodes.

Traditional rectifiers utilize diodes, mostly based on semiconductor p-n junctions with inversion symmetry broken at the interface to transform alternating current into direct current. This rectification effect can be simply written as the nonreciprocity of resistance with respect to the current direction, i.e., $R(I) \neq R(-I)$, and it has been one of the building blocks of modern semiconductor technologies. Recently, junction-free nonreciprocal electrical transport has been reported as a material's inherent property in a wide range of materials arising from different mechanisms[1–24]. It has attracted intensive research interest because of its relevance to both fundamental studies and potential applications. From a fundamental perspective, such nonreciprocal transport provides an insightful approach to study intrinsic physical

[1]School of Electrical and Electronic Engineering, Nanyang Technological University, Singapore, Singapore. [2]CINTRA CNRS/NTU/THALESUMI 3288 Research Techno Plaza, Singapore, Singapore. [3]Science, Mathematics and Technology (SMT), Singapore University of Technology and Design, Singapore, Singapore. [4]Research Laboratory for Quantum Materials, Department of Applied Physics, The Hong Kong Polytechnic University, Hong Kong, China. [5]School of Materials Science and Engineering, Peking University, Beijing, China. [6]Division of Physics and Applied Physics, School of Physical and Mathematical Sciences, Nanyang Technological University, Singapore, Singapore. [7]Interdisciplinary Center for Theoretical Physics and Information Sciences (ICTPIS), Fudan University, Shanghai, China. [8]School of Materials Science and Engineering, Nanyang Technological University, Singapore, Singapore. [9]These authors contributed equally: Ruihan Wang, Haoyun Chen, Hui Wang. ✉e-mail: shengyuan.yang@polyu.edu.hk; peng.song@ntu.edu.sg

properties, such as symmetry breaking[9–14], spin-orbit coupling[15,16], chirality[17,18], quantum geometry[19–24], etc. In terms of potential application, such junction-free nonreciprocal transport recently has been used for terahertz sensing[8], broadband frequency mixing[25] and high-performance energy harvesting[26].

While the nonreciprocal transport has been widely reported, its active control has turned out to be more challenging. So far, several ways have been demonstrated to manipulate nonreciprocal transport, with electrostatic gating[19,20,22–24], altering field angles[18], switching magnetic polarization[5,14,21–24], etc. Despite these progresses, a key manipulation capability that has not been established for nonreciprocal transport, but is highly desired, is the nonvolatile electrical switching of the direction of nonreciprocity. One possible way to achieve it is through coupling nonreciprocal transport with a nonvolatile electric field, e.g., a ferroelectric field. However, it turns out fundamentally challenging because the nonreciprocal transport in noncentrosymmetric material is typically associated with metallicity, which is incompatible with ferroelectricity due to the strong screening effect of their free carriers[14,27–29]. The recent discovery of sliding ferroelectricity in two-dimensional metallic materials[30–33] provides an efficient route to achieve the electric switching of structural polarity through ferroelectric coupling. Such ferroelectricity has been shown to critically influence symmetry-dependent physical properties in a material, leading to direct nonvolatile control of these properties[34–36]. Due to the unique combination of intrinsic semi-metallic property[37,38] and room temperature ferroelectricity[31–33], two-dimensional WTe_2 serves as a great platform to explore the effects of ferroelectricity-coupled structural polarity on nonreciprocal transport. Moreover, the strong spin-orbit coupling[39] and nontrivial band structure[40,41] in WTe_2 also give rise to chiral Berry curvature monopoles near the Weyl points, which leads to giant enhancement in its nonreciprocity[11–13].

WTe_2 crystallizes in the $Pmn2_1$ point group, with inversion symmetry broken along z-axis, giving rise to a structural polar axis along out-of-plane direction (Fig. 1a). This structural polarity in WTe_2 is coupled with ferroelectric polarity, which can be electrically switched by using a dual gate device configuration (Fig. 1b). Additionally, when the time reversal symmetry is broken by an external magnetic field, the nonreciprocal resistance of the polar metal can be expressed as:

$$R(I,H) = R_0(1+\beta H^2 + \gamma(P\times H)\cdot I) \quad (1)$$

Where R_0 is the ordinary resistance, β is the normal magnetoresistance coefficient, and γ is a coefficient of the nonreciprocal transport. When ferroelectric polarization is along the +z direction (denoted as P↑ in the following text) and magnetic field is applied perpendicular to the polar axis and current, the nonreciprocity of the system causes $I^- > I^+$, or $R(I^-) < R(I^+)$ (Fig. 1c, d). When the polarization is switched to the -z direction (denoted as P↓ in the following text) by dual gate voltages, the ferroelectricity-coupled structural polarity switching causes nonreciprocity to switch sign, that is, $I^- < I^+$, or $R(I^+) < R(I^-)$ (Fig. 1c, d). The vector-product-type nonreciprocal term can be experimentally probed by second harmonic measurements (Fig. 1e), which reaches maximum when the polar axis, magnetic field, and current are orthogonal to each other ($\theta = \varphi = 90°$). Using nonlinear transport measurements, we explicitly observe reversed nonreciprocal transport in few-layer WTe_2 upon electrical switching of its ferroelectric

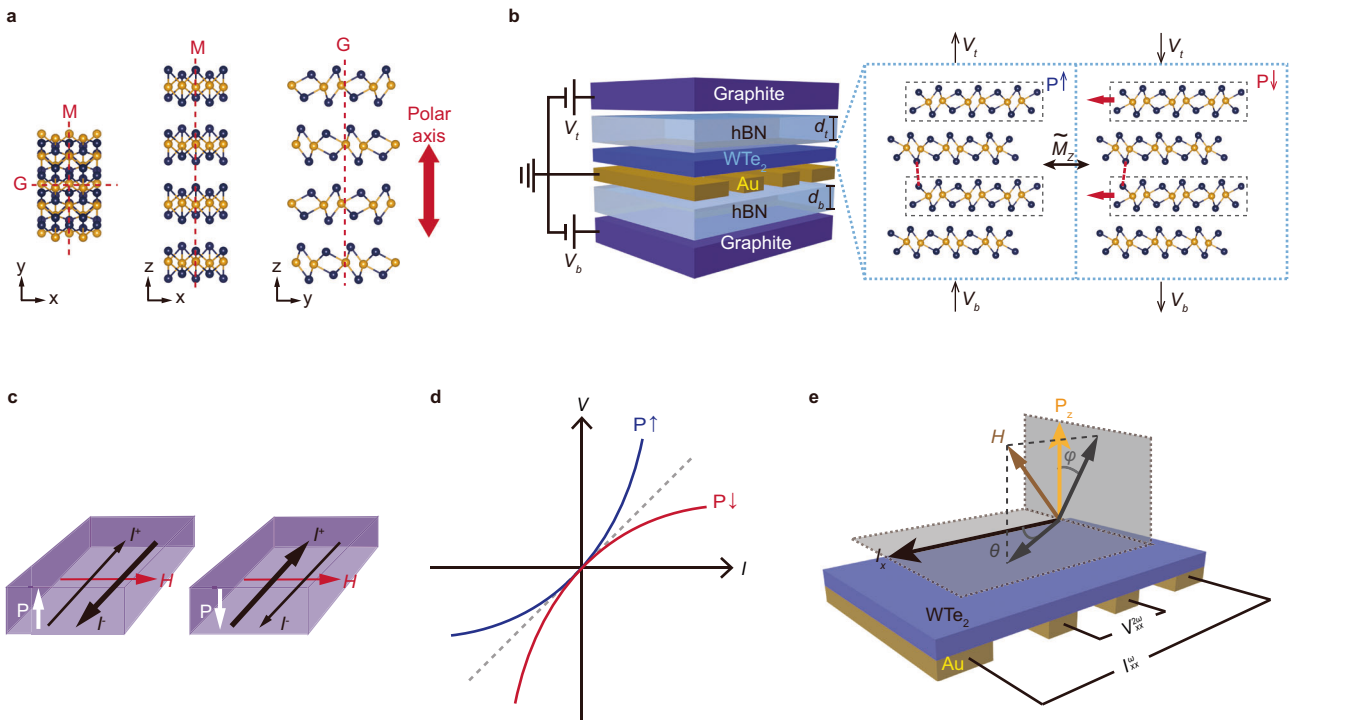

Fig. 1 | Ferroelectric polarization and polarization induced nonreciprocal transport in WTe_2. a Crystal structure of tetralayer WTe_2, with mirror plane *M* and the gliding plane *G* labeled by red dashed lines, respectively. The polar axis along z-axis is labeled by the red arrow. **b** Schematic illustration of a dual gate device structure. Gate voltages V_t and V_b can be independently applied to the top and bottom graphite, respectively. When applying both gate voltages along z direction, the vertical electrical field drives an interlayer sliding (shown as red arrow) through a mirror operation $\widetilde{M}_z$ and realizes the switching of ferroelectricity as well as structural polarity. The figure is created partly with VESTA[58]. **c** Schematic of the coupling between ferroelectric polarization and nonreciprocal transport. Under an applied in-plane magnetic field *H*, the ferroelectric polarity of the system causes nonreciprocity that manifests as $I^+ \neq I^-$, and this nonreciprocity can be reversed by reversing the ferroelectric polarity of the system. **d** The d.c. *I*–*V* characteristic of the rectification effect in WTe_2. The nonreciprocal transport in WTe_2 causes a rectification effect on current, reflected as a nonlinear IV curve, that switches sign when ferroelectricity is switched from P↑ to P↓. **e** Measurement schematic of nonreciprocal transport in noncentrosymmetric polar system, second harmonic voltage $V_{xx}^{2\omega}$ is probed while applying an a.c. current I_{xx}^{ω} along longitudinal x direction. Angle θ and φ denotes the direction of magnetic field *H* with respect to the y- and z-axis, respectively.

https://doi.org/10.1038/s41467-025-66464-7

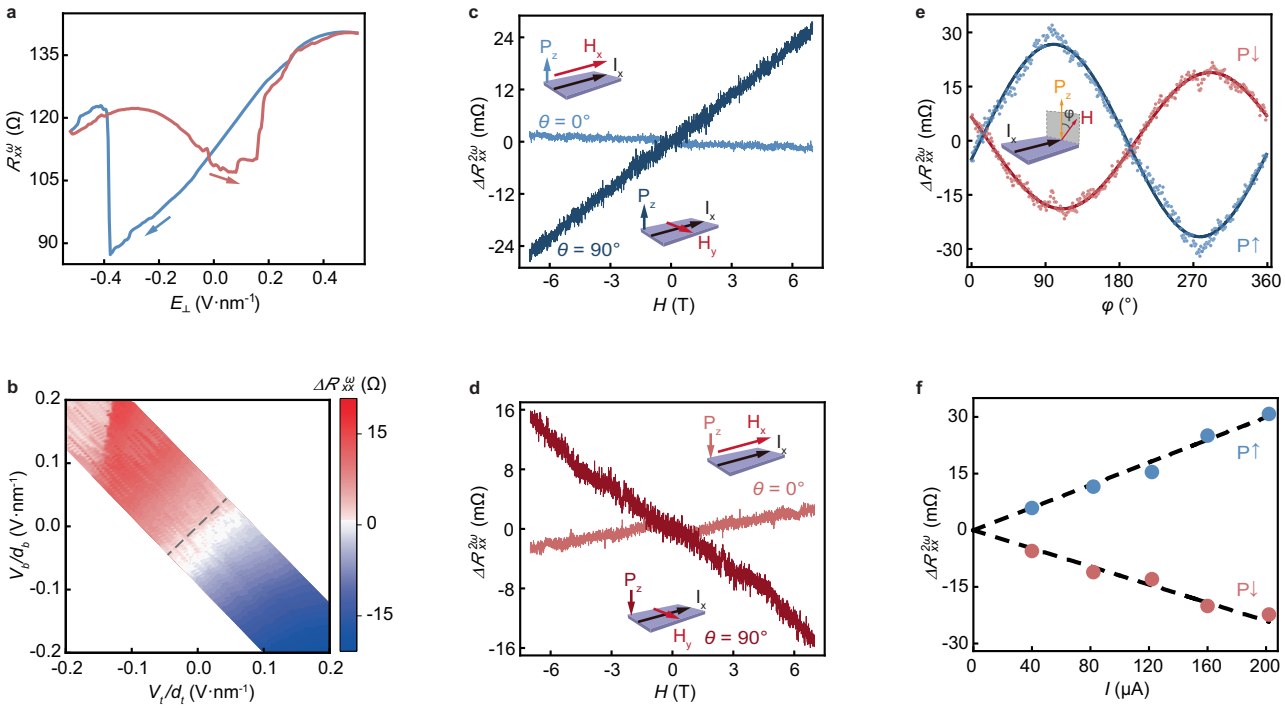

Fig. 2 | Switchable nonreciprocal magnetoresistance in tetralayer WTe_2. a First-order longitudinal resistance R_{xx}^{ω} under sweeping vertical electrical field $E_{\perp}$. Arrows denote sweeping direction. **b** Dual gate mapping of resistance difference between two opposite sweeping directions. The black dashed line is a trace of $E_{\perp} = 0$. Magnetic field dependence of $\Delta R_{xx}^{2\omega}$ at **c** positive polarization P↑ and **d** negative polarization P↓ under zero electrical field and zero net doping. $\theta = 90°$ corresponds to magnetic field H along y direction, perpendicular to the current. $\theta = 0°$ corresponds to the magnetic field H along x direction, parallel to the current. Insets denote the relative orientation between the current magnetic field and polar axis. **e** Angular dependence of $\Delta R_{xx}^{2\omega}$ when sample rotates within the yz plane for the two ferroelectric polarizations, shown by the shaded area in the inset. The solid lines are $\sin\varphi$ fittings of the data. **f** $\Delta R_{xx}^{2\omega}$ under different applied a.c. current I for the two ferroelectric polarizations. The dashed lines are linear fittings of the data. All measurements were performed at 2 K.

polarization. Moreover, the switching is nonvolatile and can be retained without external voltages. By overcoming the fundamental barrier imposed by incompatibility between ferroelectric field and metallic transport, our demonstrations establish a highly relevant control scheme for nonreciprocal physics and electronics.

Results

Electrical switching of nonreciprocal transport in WTe_2

To effectively control the ferroelectricity in WTe_2, we implemented the dual gate configuration where few-layer WTe_2 flake is sandwiched between two graphite/boron nitride (hBN) gates with hBN thickness d_t and d_b (Fig. 1b). The vertical electrical field along the out-of-plane direction can be calculated by:

$$E_{\perp} = \frac{(-V_t/d_t + V_b/d_b)}{2} \tag{2}$$

And the net electron doping of the sample is given by:

$$n_e = \frac{\varepsilon_{hBN}\varepsilon_0(V_t/d_t + V_b/d_b)}{e} \tag{3}$$

Where $\varepsilon_{hBN} \approx 3.5$ is the relative permittivity of hBN. By applying dual gate voltages simultaneously according to the equations above, we can achieve independent control over electrical field and charge doping in WTe_2.

We use standard 4-probe technique to measure both first (V_{xx}^{ω}) and second ($V_{xx}^{2\omega}$) harmonic longitudinal voltages under a.c. current I_{xx}^{ω} (Fig. 1e). The resistance of sample at first and second harmonic degree can be calculated by:

$$R_{xx}^{n\omega} = V_{xx}^{n\omega}/I_{xx}^{\omega}(n = 1, 2) \tag{4}$$

During measurement, an a.c. current $I_{xx}^{\omega} = I_0 \sin(\omega t)$ passes through the sample while applying an magnetic field H, and the magnetoresistance corresponding to the nonreciprocal transport contribution can be derived by:

$$\Delta R_{xx}^{2\omega} = \frac{\gamma R_0 H I_0 \sin\theta \sin\varphi}{2} \tag{5}$$

We systematically studied the nonvolatile electrically switchable nonreciprocal transport in trilayer, tetralayer and pentalayer WTe_2 in devices D1, D2 and D3, respectively. The results are mostly similar across different devices, and we discuss the data from tetralayer WTe_2 in the main text and the other two in Supplementary Information (Sections S5 and S6). The details of all devices are summarized in Supplementary Information S1, and we note that current is injected mostly along crystal a-axis in all devices, as confirmed by our scanning tunneling electron microscopy (STEM) measurement results.

We first confirm the ferroelectricity of tetralayer WTe_2 by measuring the vertical electrical field dependence of first-order longitudinal resistance R_{xx}^{ω} at 2 K. Figure 2a shows the butterfly shaped hysteresis loop in R_{xx}^{ω} due to ferroelectric polarization switching, consistent with previous report[31]. This butterfly shaped hysteresis behavior can be explained by the perturbation of conductance upon internal electrical field switching, causing a sudden resistance jump upon polarization switching[31]. The ferroelectric polarization switching from P↑ to P↓ (P↓ to P↑) can be achieved with a critical field $E_{\perp}$ of −0.4 V nm^{-1} (+0.2 V nm^{-1}). The asymmetric critical fields can be

https://doi.org/10.1038/s41467-025-66464-7

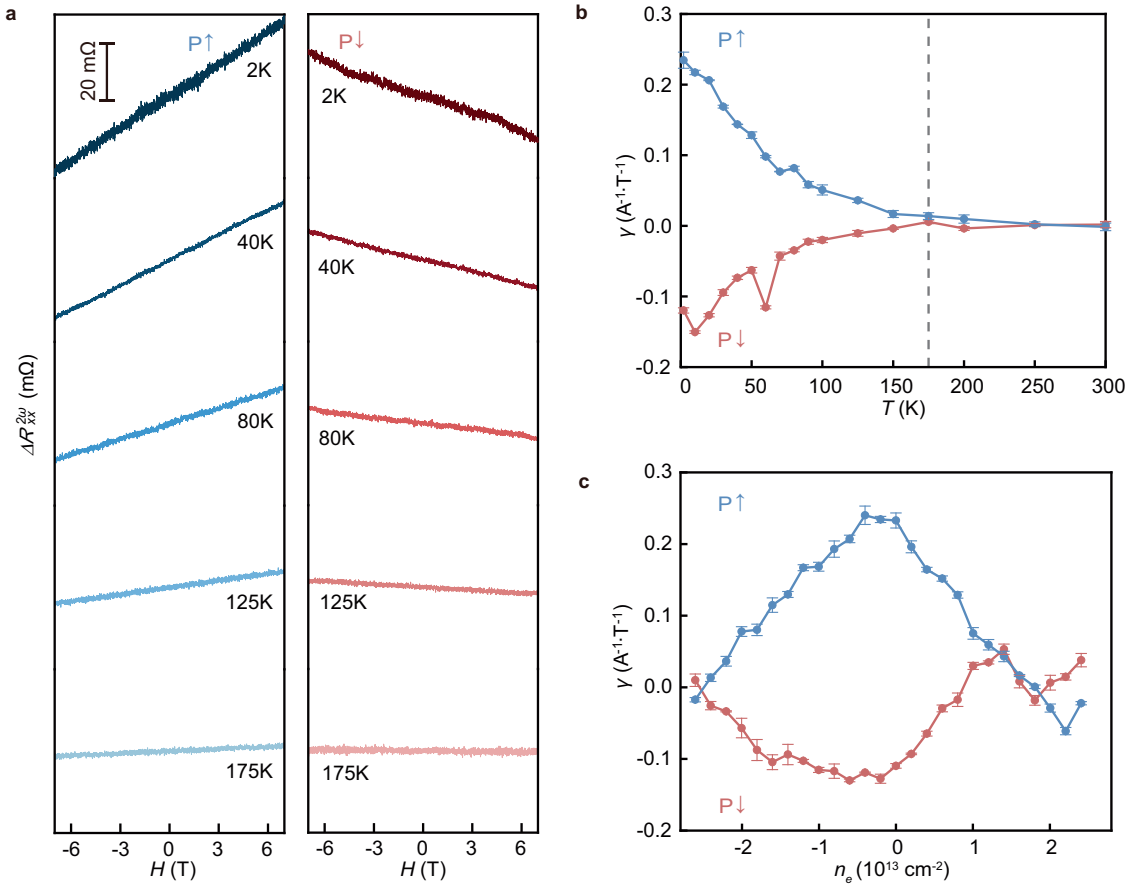

Fig. 3 | Temperature and doping dependence of nonreciprocal magnetoresistance in tetralayer WTe_2. **a** Magnetic field dependence of $\Delta R_{xx}^{2\omega}$ under P↑/ P↓ polarizations at different temperatures from 2 to 175 K. **b** Temperature dependence of nonreciprocal coefficient γ at $n_e = 0$. The dashed line denotes 175 K. **c** Electron doping dependence of nonreciprocal coefficient γ at 2 K with $E_\perp = 0$. The error bars in **b**, **c** represent uncertainties in deriving the value γ.

ascribed to a small built-in field during fabrication of the heterostructure device[35] or charge trapping effect between sample-barrier surfaces[31,42]. We also performed dual gate mappings on R_{xx}^{ω} to comprehensively showcase the ferroelectricity of WTe_2. Figure 2b plots the dual gate mapping of the difference of resistance between two opposite sweeping directions, written as ΔR_{xx}^{ω}. The result shows butterfly shaped hysteresis behavior throughout the center hysteretic region that also resembles previous report[31].

We then performed nonreciprocal transport measurements under both ferroelectric polarizations. To achieve nonvolatile electrical control of the polarization, the ferroelectric polarization is preset to P↑ (P↓) state by sweeping vertical electrical field to maximum value along +z (−z) direction then returning to $E_\perp = 0$. Under an a.c. current $I = 200$ μA, the second harmonic resistance $R_{xx}^{2\omega}$ of sample under P↑ state is measured while the in-plane magnetic field is applied either perpendicular ($\theta = 90°$) or parallel ($\theta = 0°$) to the current. The second harmonic signal is antisymmetrized with respect to magnetic field to extract the second harmonic nonreciprocal magnetoresistance $\Delta R_{xx}^{2\omega}$ and rule out any field-independent contributions (See Supplementary Information S3 for details of the antisymmetrization process). We observe a nearly linear field dependence of $\Delta R_{xx}^{2\omega}$ to magnetic field when $\theta = 90°$ and vanished signal when $\theta = 0°$ (Fig. 2c), which are consistent with Eq. 5 and are direct evidence of the nonreciprocal transport in WTe_2 dedicated to structural polarity.

Most importantly, when the ferroelectric polarization is reversed to P↓ state, the field dependence of $\Delta R_{xx}^{2\omega}$ at $\theta = 90°$ shows opposite slope (Fig. 2d), indicating a sign reversal of the nonreciprocity in WTe_2 and a clear coupling between ferroelectric polarization switching and direction of nonreciprocal transport. The absence of external voltage in all the measurements (Fig. 2c, d) demonstrate the nonvolatile nature of the nonreciprocity switching. Such nonvolatile electrical switching of nonreciprocal transport has not been demonstrated before and establishes a key component for future exploitation of junction-free nonreciprocal electronics.

The switchable nonreciprocal transport is further proved with rotating magnetic field and varying injection current. Figure 2e shows the field angle dependence of $\Delta R_{xx}^{2\omega}$ when sample is rotated in yz plane under constant magnetic field of 7 T. We note that in a few-layer WTe_2, the inversion symmetry along in-plane a-axis is also broken, creating an in-plane polar axis[41]. This in-plane polar axis can lead to a second harmonic signal under out-of-plane field. For the clarity of demonstration, the signal due to this fixed in-plane polarization is removed (see Supplementary Information S4 for details of the process) and the angle dependence plot only shows the contribution of the out-of-plane ferroelectric polar axis. The $\Delta R_{xx}^{2\omega}$ under both ferroelectric polarizations shows a one-fold dependence of field angle that agrees well with $\sin\varphi$ relation. Figure 2f shows the $\Delta R_{xx}^{2\omega}$ under both ferroelectric polarizations under different injection currents, the signal scales linearly with I and the sign reversal feature is observed for all current amplitudes. All results above provide direct justification for the existence of polarity-induced nonreciprocal transport in tetralayer WTe_2 and its signal reversal upon ferroelectric switching.

https://doi.org/10.1038/s41467-025-66464-7

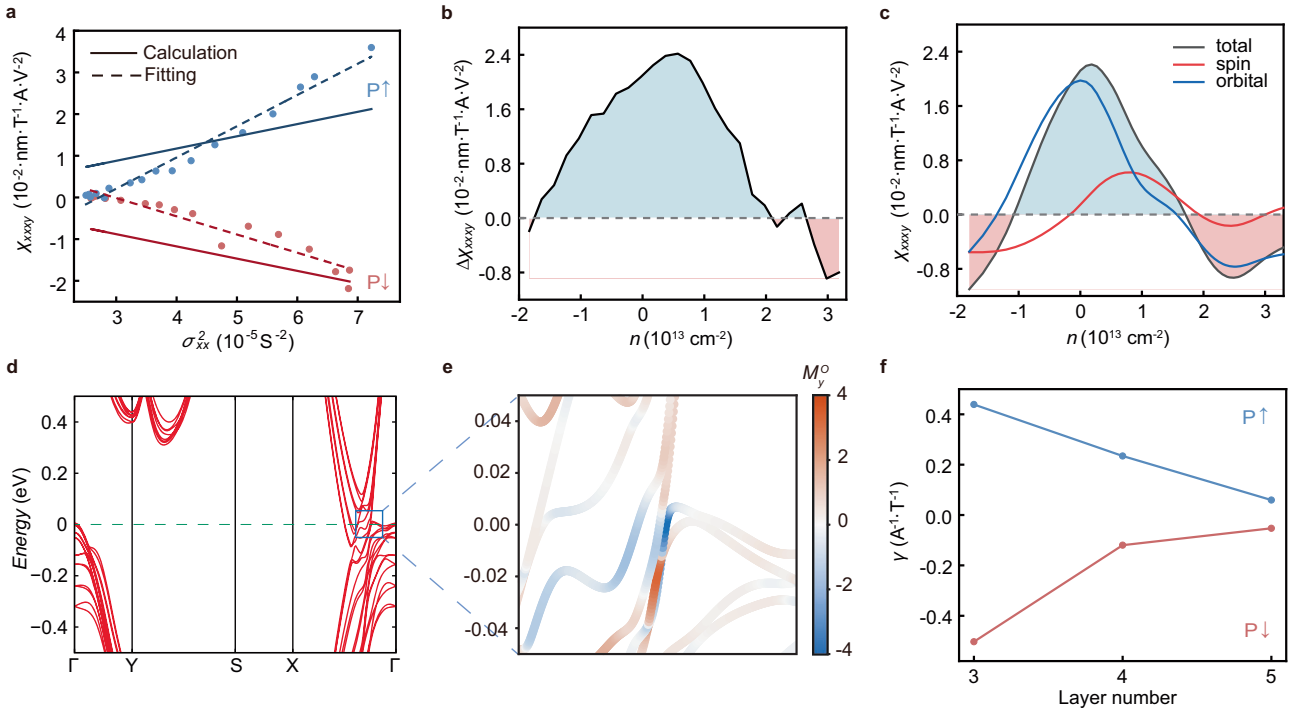

Fig. 4 | Microscopic origin and layer dependence of nonreciprocal magnetoresistance in WTe_2. **a** Nonlinear conductivity tensor element χ_{xxxy} as a function of σ^2_{xx} for the two ferroelectric polarizations. The data points represent experimental results, linearly fitted by the dashed lines, and the solid lines denote theoretical calculations for the respective polarization states. **b** Antisymmetrized nonlinear conductivity $\Delta\chi_{xxxy}$ at 2 K as a function of carrier density n, representing the signal from P↑ state. **c** Calculated nonlinear response χ_{xxxy} as a function of n for P↑ at 2 K. The total contribution and the contributions from spin and orbital magnetic moment are plotted separately. **d** Band structure of tetralay**e**r WTe_2 with spin-orbit coupling. **e** Momentum-resolved distribution of the y-component of the orbital magnetic moment M^O_y in the band structure. A pronounced enhancement of the orbital magnetic moment is observed near the Fermi level, particularly around band small-gap regions. **f** Layer dependence of nonreciprocal coefficient γ of trilayer, tetralayer and pentalayer WTe_2 at 2 K.

Temperature and doping dependence of the nonreciprocal magnetoresistance

Next, we investigate the temperature dependence of the nonreciprocal magnetoresistance when magnetic field is swept along y direction ($\theta = 90°$). Under all temperatures, $\Delta R^{2\omega}_{xx}$ remains linear to field (Fig. 3a), but the signal slope decreases monotonically with increasing temperature, before vanishing at ~175 K. To show the strength of the nonreciprocity in WTe_2, we have extracted the nonreciprocal coefficient based on Eq. 5 as:

$$\gamma = \frac{2\Delta R^{2\omega}_{xx}}{R_0 H I_0} \tag{6}$$

At 2 K, the maximum nonreciprocal coefficient is calculated to be ~0.23/−0.15 A^{-1} T^{-1} for P↑/P↓ polarizations, comparable with previous reports on bulk systems with large nonreciprocal signal[10,15]. Comparing signals of the two ferroelectric polarizations, we note that γ remains opposite sign and similar magnitude in all measured temperatures until vanishing at ~175 K (Fig. 3b), suggesting the same origin of the nonreciprocal transport under opposite ferroelectric polarizations.

Moreover, the observed nonreciprocal magnetoresistance can be effectively modulated by varying carrier density, which allows us to electrically control the nonreciprocal transport by means of electrostatic doping. The dual gate is controlled to scan along the $E_\perp = 0$ trace in the dual gate ΔR_{xx} mapping, so to maintain the ferroelectric polarization undisturbed while changing the doping. Figure 3c shows that the nonreciprocal coefficient γ of P↑ and P↓ states. The nonreciprocal response under both polarizations can be effectively tuned by doping. Under light hole doping region, signals under both ferroelectric polarizations are enhanced while maintaining opposite sign relation. Under both high electron and hole doping, signal rapidly decreases to nearly zero. Our calculation results further confirm this large doping dependence, which is discussed in detail in the next section.

Theory of nonreciprocal magnetoresistance in WTe_2

The nonlinear conductivity tensor (χ_{abcd}) of the nonreciprocal magnetotransport is defined by (repeated Cartesian indices are summed over):

$$j_a = \chi_{abcd} E_b E_c H_d \tag{7}$$

where j_a is nonlinear current density along a; E_b, E_c and H_d are electrical field along b, electrical field along c, and magnetic field along d, respectively.

Under the constraint of C_s symmetry, which applies to few-layer WTe_2, the tensor elements χ_{xxxy} and χ_{yyyx} are allowed for the planar transport setup, while components χ_{xxxx} and χ_{yyyy} are forbidden by symmetry. In our experiment, the driving current is applied along the x direction (a-axis), so only χ_{xxxy} is relevant.

For this nonreciprocal transport coefficient χ_{xxxy}, the leading order contribution is proportional to τ^2 (τ is the relaxation time). It is often called the Drude-like contribution, because it originates from the out-of-equilibrium distribution that is second order in the driving field $\delta f \propto \tau^2 E^2$. Note that the nonreciprocal current from this δf must vanish under time reversal symmetry, so the planar H field is necessary: its role is to break time reversal symmetry, by effectively magnetizing the system via coupling to spin and orbital magnetic moments of electrons. Indeed, our experimental data of χ_{xxxy} exhibits a linear scaling with σ^2_{xx} ($\propto \tau^2$) (Fig. 4a), which confirms this physical picture.

This Drude-like nonreciprocal coefficient can be evaluated from Eq. 8[43]:

$$\chi^{D}_{abcd} = \tau^2 \sum_n \int [dk] f'_0 [(\partial_b \partial_a \mathscr{M}^n_d) v^n_c - (\partial_c \partial_b v^n_a) \mathscr{M}^n_d] \quad (8)$$

Here, n is the band index, f_0 is the equilibrium Fermi distribution, $\partial_a \equiv \partial_{k_a}$, $v^n_c = \partial_c \varepsilon_n$, $\mathscr{M}^n_d$ is magnetic moment of a Bloch state, which includes both the spin and the orbital contributions (see "Methods"). Based on this formula, we perform first-principles calculations to evaluate χ_{xxxy} for few-layer WTe_2. In our calculations, the value of τ as a function of temperature T is extracted from the experimental data of σ_{xx} combined with an estimation of Drude weight (see Supplementary Information S4 for temperature dependence of σ_{xx}), and there is no fitting parameter involved.

Figure 4a shows the scaling plot of nonlinear conductivity χ_{xxxy} extracted from experiment data according to

$$\chi_{xxxy} = \frac{\sigma_{xx} \Delta E^{2\omega}_{xx}}{E^2_{xx} H} \quad (9)$$

and plotted as a function of σ^2_{xx}. The solid lines are the theoretical results. As mentioned, the experimental data exhibits a nice linear relationship, consistent with the $\chi \propto \tau^2$ scaling from the nonreciprocal Drude-like mechanism. The theoretical results also show excellent agreement with experiment: it gives the correct sign, trend, and order of magnitude, compared to experimental data. The small deviation at low conduction end could be caused by the shift of the Fermi level at high temperatures[12,44,45].

The large doping dependence in our experiment also finds excellent agreement with calculation results, which provide further insights into the origin of the observed large nonreciprocal transport. For the tetralayer WTe_2, the two opposite ferroelectric states are related by a glide mirror operation $\tilde{M}_z$. As a result, tensor elements, such as χ_{xxxy} and χ_{yyyx} reverse sign between the two ferroelectric states. Therefore, in the following, we focus only on the tensor elements for the upward-polarized ferroelectric state, and the experiment results are antisymmetrized as:

$$\Delta\chi_{xxxy} = \frac{(\chi_{xxxy,\,P\uparrow} - \chi_{xxxy,\,P\downarrow})}{2} \quad (10)$$

Figure 4b shows the experimental result of $\Delta\chi_{xxxy}$, in which the enhancement of nonlinear conductivity is observed near the intrinsic Fermi level and reaches maximum in the light electron doping level. Figure 4c shows the calculated doping dependence of the nonlinear conductivity, also showing a pronounced enhancement near intrinsic Fermi level. The agreement with the experimental results is remarkable, both in trend and in the magnitude, offering a strong support for our theoretical interpretation.

More importantly, theoretical analysis reveals a significant geometric contribution in the nonreciprocal Drude mechanism. As we mentioned above, the coupling of in-plane H field to electrons is via both the spin ($\mathcal{M}^S$) and the orbital ($\mathcal{M}^O$) magnetic moments, i.e., $\mathcal{M} = \mathcal{M}^S + \mathcal{M}^O$. While the spin moment is bounded and usually has less variations in magnitude, the orbital moment strongly depends on band structure and is greatly enhanced at band near degeneracies. This enhancement is a manifestation of interband coherence, similar to other band geometric quantities like Berry curvature and Berry connection polarizability. As a semimetal, the conduction and valence bands of WTe_2 overlaps around the Fermi energy, making a good opportunity for enhanced orbital moment $\mathcal{M}^O$ and hence for promoting the nonreciprocal transport. In Fig. 4c, we separate the contributions from spin and orbital magnetic moments. Indeed, we observe that the orbital part is the dominant source of this enhancement. In Fig. 4d, we plot the band structure of tetralayer WTe_2, along with the value of orbital magnetic moment $\mathcal{M}^O_y$ in Fig. 4e. It confirms the significant enhancement of orbital magnetic moment around band near degeneracies near the Fermi level. Drude-like mechanisms are usually considered as trivial compared to other mechanisms involving quantum geometric properties of band structures. Our findings here offer an exception to this common wisdom, demonstrating that in nonreciprocal magneto-transport, the Drude-like mechanism may also encode geometric information of band structures.

Different from even-layer WTe_2, the sliding geometry that relates the two ferroelectric states in odd-layer WTe_2 is an inversion operation I. To investigate the effect of layer number on the nonreciprocal magnetoresistance of WTe_2, we compared the nonreciprocal coefficient γ of trilayer, tetralayer and pentalayer WTe_2, as shown in Fig. 4f. In all devices, the nonreciprocal magnetoresistance shows opposite sign, indicating that the electrical switching of nonreciprocal transport is independent of layer number. However, as layer number increases from trilayer to pentalayer, the signal magnitude shows a monotonic decrease, which can be ascribed to the stronger Coulomb screening effect in thicker samples with higher carrier density and conductivity[46,47].

Discussion

Nonvolatile electrical control has been pursued widely as a highly important tuning knob for various device physics[30,48,49]. In this study, we have achieved nonvolatile electrical switching of nonreciprocal transport in few-layer ferroelectric polar metal WTe_2. The direction of nonreciprocity can be deterministically switched by ferroelectric field and its magnitude can be broadly tuned with electrostatic doping. Our study establishes a key tuning knob to further advance the emerging research of nonreciprocal physics and their device applications.

Using first-principles calculations, we show that the main contribution of the observed nonreciprocal transport is the Drude-like term enhanced by the giant orbital magnetic moment near the intrinsic Fermi level. We reveal that such Drude-like mechanism also encodes band geometric information, which is significantly enhanced by interband coherence. This is contrary to the common wisdom that Drude-like mechanism is always "trivial", in the sense that it does not manifest interband coherence like other mechanisms involving Berry curvature or Berry connection polarizability.

Methods

Device fabrication

All crystals were purchased from HQGraphene and used as received. First, hBN and graphite flakes were mechanically exfoliated on 285 nm SiO_2/Si substrates and examined by optical microscope to select the flakes with optimal thickness (graphite: 5–8 nm, hBN: 15–30 nm) and clean surface. A polycarbonate/polydimethylsiloxane stamp-assisted dry transfer technique was used to pick up the flakes and fabricate an hBN/graphite stack. Standard electron beam lithography is used to write electrode patterns on the stack, followed by e-beam deposition of 5/25 nm Ti/Au to finish bottom gate fabrication.

Few-layer WTe_2 flakes were mechanically exfoliated on SiO_2/Si substrates inside a N_2 glovebox with $O_2 < 0.2$ ppm and $H_2O < 0.1$ ppm. Graphite/hBN/WTe_2 stacks were assembled and released onto the bottom hBN/graphite stacks with the same dry transfer method in the same N_2 glovebox where WTe_2 flakes were exfoliated to finish the final devices. The assembly of Graphite/hBN/WTe_2 stacks were done immediately after exfoliation of WTe_2.

The WTe_2 flakes with specific layer number and crystal orientation were first selected based on their optical contrast and long, straight edges, respectively. The thickness of hBN layer is characterized later by atomic force microscopy (AFM) while the layer number and crystallography information of WTe_2 is confirmed by STEM after the

transport measurements (see Supplementary Information S1 for AFM and STEM characterization results).

Electrical transport measurements

Electrical measurements were performed in the Oxford Teslatron cryostat with a base temperature of 2 K and a magnetic field up to 7 T. A Keithley 6430 source meter and a Keithley 2401 source meter were used to provide DC gate voltage to top and bottom gates, respectively. First and second harmonic signals are collected simultaneously using standard lock-in technique with two SR830 lock-in amplifiers under frequency 13.317 Hz. The phases of first (second) harmonic signal were close to 0° ($\pm 90^\circ$), consistent with expectations.

Theoretical calculations

To evaluate the nonlinear response of WTe_2, we performed first-principles calculations based on density functional theory using the projector augmented wave method[50], as implemented in the Vienna ab initio simulation package[51,52]. The Perdew–Burke–Ernzerhof exchange-correlation functional was employed[53], and calculations using the optB88-vdW functional were also performed to account for van der Waals interactions[54]. A plane-wave energy cutoff of 400 eV was used. The Brillouin zone was sampled using a Γ-centered $12 \times 6 \times 1$ k-point mesh. Spin-orbit coupling was included in all calculations. Based on the obtained band structure, we constructed a Wannier tight-binding model for WTe_2 using the Wannier90 package[55–57]. The nonlinear conductivity tensor elements were then computed from the tight-binding model. To ensure numerical convergence, a dense k-mesh of $4000 \times 2000 \times 1$ was used in the Brillouin zone integration.

To separate the contribution of the spin and orbital magnetic moments in the Drude-like nonreciprocal coefficient, we calculated the spin and orbital magnetic moments using the following formula:

For spin magnetic moment:

$$\mathcal{M}^{mn} = -g\mu_B \boldsymbol{s}^{\mathbf{mn}} \tag{11}$$

For orbital magnetic moment:

$$\mathcal{M}^{mn} = \frac{1}{4i}\sum_{l\neq m,n}\left(\frac{1}{\varepsilon_l - \varepsilon_m} + \frac{1}{\varepsilon_l - \varepsilon_n}\right)\boldsymbol{v}^{\mathbf{ml}} \times \boldsymbol{v}^{\mathbf{ln}} \tag{12}$$

$\boldsymbol{s}^{\mathbf{mn}}$ ($\boldsymbol{v}^{\mathbf{ml}}$) are the matrix elements of spin (velocity) operator, μ_B is Bohr magneton, and g is the g factor.

Data availability

Supplementary Information is available for this paper. The data that support the plots within this paper are available at the Repository DR-NTU (DATA): https://researchdata.ntu.edu.sg/dataset.xhtml?persistentId=doi:10.21979/N9/KQC7B7.

References

1. Rikken, G. L. J. A., Fölling, J. & Wyder, P. Electrical magnetochiral anisotropy. *Phys. Rev. Lett.* **87**, 236602 (2001).
2. Rikken, G. L. J. A. & Wyder, P. Magnetoelectric anisotropy in diffusive transport. *Phys. Rev. Lett.* **94**, 016601 (2005).
3. Nadeem, M., Fuhrer, M. S. & Wang, X. The superconducting diode effect. *Nat. Rev. Phys.* **5**, 558–577 (2023).
4. Ando, F. et al. Observation of superconducting diode effect. *Nature* **584**, 373–376 (2020).
5. Xiong, J. et al. Electrical switching of Ising-superconducting nonreciprocity for quantum neuronal transistor. *Nat. Commun.* **15**, 1–10 (2024).
6. Suárez-Rodríguez, M. et al. Nonlinear transport in non-centrosymmetric systems. *Nat. Mater.* **24**, 1005–1018 (2025).
7. Du, Z. Z., Lu, H.-Z. & Xie, X. C. Nonlinear Hall effects. *Nat. Rev. Phys.* **3**, 744–752 (2021).
8. Xi, T. et al. Terahertz sensing based on the nonlinear electrodynamics of the two-dimensional correlated topological semimetal $TaIrTe_4$. *Nat. Electron.* **8**, 578–586 (2025).
9. Tokura, Y. & Nagaosa, N. Nonreciprocal responses from non-centrosymmetric quantum materials. *Nat. Commun.* **9**, 3740 (2018).
10. Wang, Y. et al. Gigantic magnetochiral anisotropy in the topological semimetal $ZrTe_5$. *Phys. Rev. Lett.* **128**, 176602 (2022).
11. He, P. et al. Nonlinear magnetotransport shaped by Fermi surface topology and convexity. *Nat. Commun.* **10**, 1290 (2019).
12. Yokouchi, T., Ikeda, Y., Morimoto, T. & Shiomi, Y. Giant magnetochiral anisotropy in Weyl semimetal WTe_2 induced by diverging Berry curvature. *Phys. Rev. Lett.* **130**, 136301 (2023).
13. Liu, T. et al. Crystallographically dependent bilinear magnetoelectric resistance in a thin WTe_2 layer. *Phys. Rev. B* **108**, 165407 (2023).
14. Zhang, J. et al. A correlated ferromagnetic polar metal by design. *Nat. Mater.* **23**, 912–919 (2024).
15. Ideue, T. et al. Bulk rectification effect in a polar semiconductor. *Nat. Phys.* **13**, 578–583 (2017).
16. Li, Y. et al. Nonreciprocal charge transport up to room temperature in bulk Rashba semiconductor α-GeTe. *Nat. Commun.* **12**, 540 (2021).
17. Yan, B. Structural chirality and electronic chirality in quantum materials. *Annu. Rev. Mater. Res.* **54**, 97–115 (2024).
18. Guo, C. et al. Switchable chiral transport in charge-ordered Kagome metal CsV_3Sb_5. *Nature* **611**, 461–466 (2022).
19. Yasuda, K. et al. Large non-reciprocal charge transport mediated by quantum anomalous Hall edge states. *Nat. Nanotechnol.* **15**, 831–835 (2020).
20. Legg, H. F. et al. Giant magnetochiral anisotropy from quantum-confined surface states of topological insulator nanowires. *Nat. Nanotechnol.* **17**, 696–700 (2022).
21. Zhao, W. et al. Magnetic proximity and nonreciprocal current switching in a monolayer WTe_2 helical edge. *Nat. Mater.* **19**, 503–507 (2020).
22. Zhang, Z. et al. Controlled large non-reciprocal charge transport in an intrinsic magnetic topological insulator $MnBi_2Te_4$. *Nat. Commun.* **13**, 6191 (2022).
23. Wang, N. et al. Quantum-metric-induced nonlinear transport in a topological antiferromagnet. *Nature* **621**, 487–492 (2023).
24. Gao, A. et al. An antiferromagnetic diode effect in even-layered $MnBi_2Te_4$. *Nat. Electron.* **7**, 751–759 (2024).
25. Min, L. et al. Colossal room-temperature non-reciprocal Hall effect. *Nat. Mater.* **23**, 1671–1677 (2024).
26. Hu, F. et al. Ultrabroadband nonlinear Hall rectifier using SnTe. *Nat. Nanotechnol.* 1–8 (2025).
27. Anderson, P. W. & Blount, E. I. Symmetry considerations on martensitic transformations: "ferroelectric" metals? *Phys. Rev. Lett.* **14**, 217–219 (1965).
28. Shi, Y. et al. A ferroelectric-like structural transition in a metal. *Nat. Mater.* **12**, 1024–1027 (2013).
29. Kim, T. et al. Polar metals by geometric design. *Nature* **533**, 68–72 (2016).
30. Jindal, A. et al. Coupled ferroelectricity and superconductivity in bilayer T_d-$MoTe_2$. *Nature* **613**, 48–52 (2023).
31. Fei, Z. et al. Ferroelectric switching of a two-dimensional metal. *Nature* **560**, 336–339 (2018).
32. Sharma, P. et al. A room-temperature ferroelectric semimetal. *Sci. Adv.* **5**, eaax5080 (2019).
33. Yang, Q., Wu, M. & Li, J. Origin of two-dimensional vertical ferroelectricity in WTe_2 bilayer and multilayer. *J. Phys. Chem. Lett.* **9**, 7160–7164 (2018).
34. Xiao, J. et al. Berry curvature memory through electrically driven stacking transitions. *Nat. Phys.* **16**, 1028–1034 (2020).
35. Kang, K. et al. Switchable moiré potentials in ferroelectric WTe_2/WSe_2 superlattices. *Nat. Nanotechnol.* **18**, 861–866 (2023).

36. Nishijima, T. et al. Ferroic Berry curvature dipole in a topological crystalline insulator at room temperature. *Nano Lett.* **23**, 2247–2252 (2023).
37. Soluyanov, A. A. et al. Type-II Weyl semimetals. *Nature* **527**, 495–498 (2015).
38. Li, P. et al. Evidence for topological type-II Weyl semimetal WTe_2. *Nat. Commun.* **8**, 2150 (2017).
39. Jiang, J. et al. Signature of strong spin-orbital coupling in the large nonsaturating magnetoresistance material WTe_2. *Phys. Rev. Lett.* **115**, 166601 (2015).
40. Ali, M. N. et al. Large, non-saturating magnetoresistance in WTe_2. *Nature* **514**, 205–208 (2014).
41. Kang, K., Li, T., Sohn, E., Shan, J. & Mak, K. F. Nonlinear anomalous Hall effect in few-layer WTe_2. *Nat. Mater.* **18**, 324–328 (2019).
42. Hao, T. et al. Coupling effects of interface charge trapping and polarization switching in HfO_2-based ferroelectric field effect transistors. *APL Mater.* **12**, 011108 (2024).
43. Huang, Y.-X. et al. Nonlinear current response of two-dimensional systems under in-plane magnetic field. *Phys. Rev. B* **108**, 075155 (2023).
44. Wu, Y. et al. Temperature-induced Lifshitz transition in WTe_2. *Phys. Rev. Lett.* **115**, 166602 (2015).
45. Pletikosić, I., Ali, M. N., Fedorov, A. V., Cava, R. J. & Valla, T. Electronic structure basis for the extraordinary magnetoresistance in WTe_2. *Phys. Rev. Lett.* **113**, 216601 (2014).
46. Ji, H. et al. Tunable mobility in double-gated $MoTe_2$ field-effect transistor: effect of coulomb screening and trap sites. *ACS Appl. Mater. Interfaces* **9**, 29185–29192 (2017).
47. Hintermayr, V. A., Polavarapu, L., Urban, A. S. & Feldmann, J. Accelerated carrier relaxation through reduced coulomb screening in two-dimensional halide perovskite nanoplatelets. *ACS Nano* **12**, 10151–10158 (2018).
48. Noël, P. et al. Non-volatile electric control of spin–charge conversion in a $SrTiO_3$ Rashba system. *Nature* **580**, 483–486 (2020).
49. Huang, X. et al. Manipulating chiral spin transport with ferroelectric polarization. *Nat. Mater.* **23**, 898–904 (2024).
50. Blöchl, P. E. Projector augmented-wave method. *Phys. Rev. B* **50**, 17953–17979 (1994).
51. Kresse, G. & Hafner, J. Ab initio molecular-dynamics simulation of the liquid-metal-amorphous-semiconductor transition in germanium. *Phys. Rev. B* **49**, 14251–14269 (1994).
52. Kresse, G. & Furthmüller, J. Efficient iterative schemes for ab initio total-energy calculations using a plane-wave basis set. *Phys. Rev. B* **54**, 11169–11186 (1996).
53. Perdew, J. P., Burke, K. & Ernzerhof, M. Generalized gradient approximation made simple. *Phys. Rev. Lett.* **77**, 3865–3868 (1996).
54. Klimeš, J., Bowler, D. R. & Michaelides, A. Chemical accuracy for the van der Waals density functional. *J. Phys. Condens. Matter.* **22**, 022201 (2009).
55. Marzari, N. & Vanderbilt, D. Maximally localized generalized Wannier functions for composite energy bands. *Phys. Rev. B* **56**, 12847–12865 (1997).
56. Souza, I., Marzari, N. & Vanderbilt, D. Maximally localized Wannier functions for entangled energy bands. *Phys. Rev. B* **65**, 035109 (2001).
57. Mostofi, A. A. et al. Wannier90: a tool for obtaining maximally-localised Wannier functions. *Comput. Phys. Commun.* **178**, 685–699 (2008).
58. Momma, K. & Izumi, F. VESTA 3 for three-dimensional visualization of crystal, volumetric and morphology data. *J. Appl. Crystallogr.* **44**, 1272–1276 (2011).

Acknowledgements

P.S. acknowledges start-up grant support from Nanyang Technological University and Singapore Ministry of Education Academic Research Fund Tier 2 (MOE-T2EP50122-0017) and Tier 1 (RG113/21, RG130/22, RG76/25) projects. S.A.Y. acknowledges support from HK PolyU Start-up fund (P0057929). X.Z. acknowledges the National Key R&D Program of China (2024YFE0109200, 2024YFA1410000). X.R.W. acknowledges support by the Singapore Ministry of Education (MOE) Academic Research Fund (AcRF) Tier 3 grant (MOE-MOET32023-0003) "Quantum Geometric Advantage". C.X. acknowledges the support by National Natural Science Foundation of China (grant no.12574114) and the start-up funding from Fudan University.

Author contributions

P.S. conceived and supervised the project. H.C. fabricated the devices with the help of B.L. and X.C. R.W. performed the measurements with the help of Z.Y. and X.R.W., and analyzed the data. R.W. performed the AFM measurements with the help of H.C. Z.H. and X.Z. performed the STEM measurements. H.W., J.C., C.X., and S.A.Y. performed the theoretical calculations. R.W., H.C., H.W., S.A.Y., and P.S. wrote the manuscript with input from all authors. All authors discussed the results and commented on the manuscript.

Competing interests

The authors declare no competing interests.

Additional information

Supplementary information The online version contains supplementary material available at https://doi.org/10.1038/s41467-025-66464-7.

Correspondence and requests for materials should be addressed to Shengyuan A. Yang or Peng Song.

Peer review information *Nature Communications* thanks Jung-Woo Yoo and the other anonymous reviewer(s) for their contribution to the peer review of this work. A peer review file is available.